Supplementary Information

Surface electrostatics govern the emulsion stability of biomolecular condensates

Timothy J. Welsh[1,†], Georg Krainer[1,†], Jorge R. Espinosa[2,†], Jerelle A. Joseph[2], Akshay Sridhar[2], Marcus Jahnel[3,4,5], William E. Arter[1], Kadi L. Saar[1], Simon Alberti[4,*], Rosana Collepardo-Guevara[2,6,7,*], Tuomas P.J. Knowles[1,2,*]

[1] Centre for Misfolding Diseases, Yusuf Hamied Department of Chemistry, University of Cambridge, Lensfield Road, Cambridge CB2 1EW, UK

[2] Cavendish Laboratory, University of Cambridge, J J Thomson Avenue, Cambridge CB3 0HE, UK

[3] Max Planck Institute of Molecular Cell Biology and Genetics, Pfotenhauerstr. 108, 01307 Dresden, Germany

[4] Biotechnology Center (BIOTEC), Center for Molecular and Cellular Bioengineering (CMCB), Technische Universität Dresden, Tatzberg 47/49, 01307 Dresden, Germany

[5] Cluster of Excellence "Physics of Life", TU Dresden, Dresden, Germany

[6] Department of Genetics, University of Cambridge, Cambridge CB2 3EH, UK

[7] Yusuf Hamied Department of Chemistry, University of Cambridge, Lensfield Road, Cambridge CB2 1EW, UK

[†] These authors contributed equally to this work

* To whom correspondence may be addressed: Tuomas P.J. Knowles (tpjk2@cam.ac.uk), Rosana Collepardo-Guevara (rc597@cam.ac.uk), Simon Alberti (simon.alberti@tu-dresden.de)

Primary Methods

Materials. All reagents and chemicals were purchased with the highest purity available. The PR_{25} peptide, containing 25 proline–arginine repeats, was obtained from GenScript. N-terminally labelled PR_{25} was obtained by reacting the peptide with amine-reactive AlexaFluor546 (Sigma-Aldrich). PolyU RNA with a molecular weight range from 800–1,000 kDa was purchased from Sigma-Aldrich. FUS wild type and FUS G156E were produced as C-terminal EGFP fusion proteins as previously described (*10*) and stored in 50 mM Tris-HCl (pH 7.4), 500 mM KCl, 1 mM dithiothreitol, 5% glycerol. PR_{25} phase separation was induced by mixing 100 µM PR_{25} peptide with 1 mg/mL PolyU RNA in 5 mM Tris-HCl (pH 7.4). For both FUS variants, phase separation was induced by diluting the proteins to a final protein concentration of 3 µM in 25 mM KCl, 5 mM TRIS (pH 7.4). For PR_{25}:PolyU and both FUS mutants, the phase separated condensates were analyzed via µFFE within ~10 min of creation in order to minimize ageing effects; no systematic differences in zeta potential were observed across replicate samples on this time scale. 60 nm fluorescently labelled spherical gold nanoparticles (NanoPartz) were used for control measurements mentioned in Figure S4.

µFFE experiments. The design of the 3D µFFE microfluidic chip with liquid electrodes was adapted from a device previously used for studying protein charge and the separation of biomolecules (*31*, *33*). A schematic is shown in Figure S1. The device, constructed from a top and a bottom layer, was fabricated using standard single- and multilayer photolithography techniques as described in detail in the Supporting Information. Briefly, the microfluidic channels within each layer were patterned into polydimethylsiloxane (PDMS; Sylgard184, Dow Corning) using SU-8 photoresist (Microchem) on silicon masters (MicroChemicals). Top and bottom PDMS layers were then connected through plasma bonding and subsequently bonded to glass microscope slides using oxygen plasma (Diener Electronics). Devices were operated as detailed in the Supporting Information and fluids introduced using automated syringe pumps (neMESYS, Cetoni). Electric potentials were applied using a programmable 500 V power supply (Elektro-Automatik EA-PS 9500-06) and images acquired using a Zeiss AxioObserver D1 microscope. Further details are given in the Supporting Information. Image and data analysis were performed using the Fiji/ImageJ data processing software and custom-written Python scripts, respectively. Zeta potentials were calculated as described in detail in the Supporting Information.

Epifluorescence and phase-contrast microscopy in droplet stability experiments. For experiments assessing condensate emulsion stability, epifluorescence and phase contrast images were captured using

an AxioObserver D1 microscope (Zeiss) with either a 40x or 100x air objective after the specified aging time for each sample (Figure 3). Condensates were imaged within a 50 µm tall microfluidic imaging chamber in the same buffer conditions as utilized for µFFE experiments.

Optical tweezer measurements. Condensates were phase-separated in 5 mM Tris-HCl, 25 mM KCl, pH 7.4 and immediately applied to a sample chamber. Two droplets were trapped in two optical traps of the same trap stiffness. With the first trap stationary, the second trap was moved to bring the droplets into contact and initiate fusion. If fusion did not occur upon first contact as in the case of PR_{25}:PolyU condensates, the second trap was further moved to push the droplets together. As soon as coalescence initiated, the traps were kept stationary. Laser signals were recorded at 1 kHz resolution. Signals from the two traps, equal in magnitude and opposite in sign, were combined into the differential signal, from which coalescence relaxation times were deduced. A random sample of 5% of the recorded data is plotted as grey points in Figure 4. Raw data were smoothed with a Savitzky-Golay filter of 3rd order and a window of 501 points.

Fit of optical tweezer traces. The standard model for droplet fusion is based on the assumption that droplets start to coalesce as soon as their surfaces touch. This assumption holds true for many purified protein liquids (*10, 13, 14, 75*). To characterize fusion dynamics, time traces of the tweezer signal, $S(t)$, were fitted with a stretched exponential model as described previously (*14*). Briefly, the model is defined as:

$$S(t) = \begin{cases} S_{\text{offset}}, & \text{if } t < t_{\text{start}} \\ S_{\text{offset}} + (S_{\text{plateau}} - S_{\text{offset}}) \cdot [1 - \exp(-\frac{t - t_{\text{start}}}{\tau})^{\beta}], & \text{if } t \geq t_{\text{start}} \end{cases}$$

where τ denotes the relaxation time, β the stretch exponent, t_{start} the onset of fusion, S_{offset} the signal offset on the detector, and S_{plateau} the final signal value after coalescence finished.

All fusion traces (Figure 4A) have been normalized and aligned according to the start time of coalescence as deduced from the fit. Residuals from the fit were calculated for the smoothed signal. We took the maximum negative deviation from the standard model within a window of 15 seconds before the onset of fusion as a proxy for the additional energy barrier to be overcome. To quantify the fusion dynamics, the mean relaxation time was normalized by the geometric radius of the two fusing droplets.

Multiscale molecular simulations. To investigate the molecular organization of proteins, PolyU and ions within the condensates, we develop a two-step multiscale molecular simulation method. The first step

consists of coarse-grained molecular dynamics simulations of tens to hundreds of biomolecules to investigate the equilibrium ensembles of FUS and PR_{25}:PolyU condensates (see further coarse-grained simulation details in the Supporting Information). During the second step, we undertake a back-mapping procedure and perform atomistic molecular dynamics simulations with explicit solvent and ions to assess the distribution of ions in the condensed and diluted phases, and obtain magnitudes directly related to zeta potentials estimations (see details of atomistic simulations in the Supporting Information).

Supplementary Methods

Design of the μFFE device. The design of the μFFE microfluidic chip with liquid electrodes was adapted from a device previously used for studying protein charge and the separation of biomolecules (*1*, *2*). A schematic is shown in Figure S1. The device is 90 μm tall in the central electrophoresis chamber and 5 μm tall in the sample injection port. In total dimensions, the device is approximately 7 mm long and 2 mm wide. The 3D design was utilized to minimize the effect of velocity differences within the channel; further details on device design optimization are given in Saar *et al.* (*1*). For operation, the sample of interest containing phase-separated droplets is flown into the device by the central injection port where it is then surrounded by the carrier buffer solution, which was 5 mM Tris-HCl (pH 7.4) in experiments with PR_{25}:PolyU and 5 mM Tris-HCl (pH 7.4), 25 mM KCl in experiments with both FUS variants. We note that in our microfluidic technique, there is a fundamental limit to the ionic strengths that may be investigated. Salt concentrations exceeding ~30 mM within the microfluidic chip cause too little voltage drop on the condensates to reliably determine their zeta potentials. Similarly, molecular crowding cannot be carried out inside of the microfluidic device without compromising the conductive properties of the carrier buffer. On either side of the main channel, liquid electrolyte channels are filled with a constant flow of a 3 M KCl solution, supplemented with 1 mg/mL fluorescein (Sigma-Aldrich) for visualization purposes. The electrolyte solution enters the main channel via 40 μm wide and 5 μm tall electrolyte ridges, which allows for a narrow stream of electrolyte to coat both sides of the main electrophoresis channel. This solution remains under constant flow and acts as a liquid electrode, which is continually replaced. Utilization of liquid electrodes allows for high voltages to be applied as gaseous electrolysis products are flushed out of the device through the hollow electrodes (*3*). Further, the flow of electrolyte also aids in suppression of Joule heating within the device, which can be an issue with other types of micro-scale electrophoresis devices (*4*).

Fabrication of the µFFE device. Microfluidic masks were first designed using AutoCAD (Autodesk) and desired device geometries then printed on acetate transparencies (Micro Lithography Services). Polydimethylsiloxane (PDMS; DowCorning) devices were produced from SU-8 (MicroChem) molds fabricated via standard photolithographic processes by plasma bonding two individual PDMS chips to each other. Accordingly, two molds were made in order to comprise the two separate sides of the 3D microfluidic devices, with the bottom layer being produced from a single-layer (SL) replica mold, while the top layer was produced from a two-layer (TL) replica mold. Specifically, the mold for the SL chips was fabricated to a height of 45 µm and included all the structures of the devices with the exception of the protein inlet and the electrolyte bridges connecting the electrophoresis chamber and the electrolyte channels. This was achieved by spinning SU-8 3050 photoresist onto a polished silicon wafer (MicroChemicals) followed by standard soft-lithography procedures (*5*) using a custom-built LED based apparatus for performing the UV-exposure step (*6*). The fabrication of the TL replica mold for the top layer involved two subsequent lithography steps performed with SU-8 3005 and 3050 to obtain 5 and 45 µm high channels, respectively. The protein inlet as well as the connecting electrolyte bridges were featured only on the 5 µm layer, while the buffer inlet, the electrophoresis chamber, and the electrolyte channels were fabricated onto the 45 µm layer only are identical to how they appear on the SL replica mold. Feature heights on the master were assessed using a profileometer (DektakXT, Bruker). The top and bottom layer replica molds were then used to fabricate PDMS chips employing a 10:1 prepolymer-PDMS-to-curing-agent ratio (Sylgard 184, DowCorning). After degassing and curing for 3 h at 65°C, the two halves of the devices were then cut out of the molds, and holes for tubing connection (0.75 mm) and electrode insertion (1.5 mm) were created in the top layer PDMS half. Both sides of the devices were cleaned by application of Scotch tape and sonication in isopropanol. Following treatment using an oxygen plasma oven (Femto, Diener electronic) at 40% power for 30 s, the PDMS bottom layer was bonded on a glass slide with the channels facing upward. The PDMS top layer was then placed on top and carefully aligned to create a 3D device. The device was baked at 65°C for 24 h to ensure optimal bonding. Before use, devices were rendered hydrophilic via prolonged exposure to oxygen plasma (500 s, 80% power) (*7*). After this treatment, surface hydrophilicity was prolonged by immediate filling of device channels with deionized water using gel-loading tips (Fisherbrand).

Device operation and experimental conditions in µFFE experiments. The device was operated by injecting the sample solution, the carrier buffer solution, and the electrolyte solution into the corresponding inlets using automated syringe pumps (neMESYS, Cetoni). The sample was introduced

from a 100 µL glass syringe (Hamilton), other solutions were flowed from 10 mL plastic Norm-Ject syringes (Henke-Sass Wolf). All fluids were introduced to the device by 0.012x0.030" PTFE tubing (Cole-Parmer). Typical values for the flow rates were 5 µL/hr for the sample, 400–500 µL/hr for the carrier medium, and 100–250 µL/hr for the electrolyte solutions. Fluid waste was guided out of the device by tubing inserted into device outlets. Electric potentials were applied using a programmable 500 V power supply (Elektro-Automatik EA-PS 9500-06) via bent hollow metal dispensing tips (15G, Intertonics) inserted into the electrolyte outlets. The voltage was varied in linear steps, typically in the range between 0 to 80 V, using a computer controller (Raspberry Pi). Simultaneously, current readings using a digital multimeter (34401A, Agilent Technologies) were taken. Schematics of the electrical setup can be seen in Figure S2. The measurements for determining the electrical resistance of the electrodes and estimating the effective electrical potential applied across the devices were performed in an identical manner but with the sample and carrier medium replaced with 3 M KCl solution as has been described in detail earlier. All measurements were performed at room temperature.

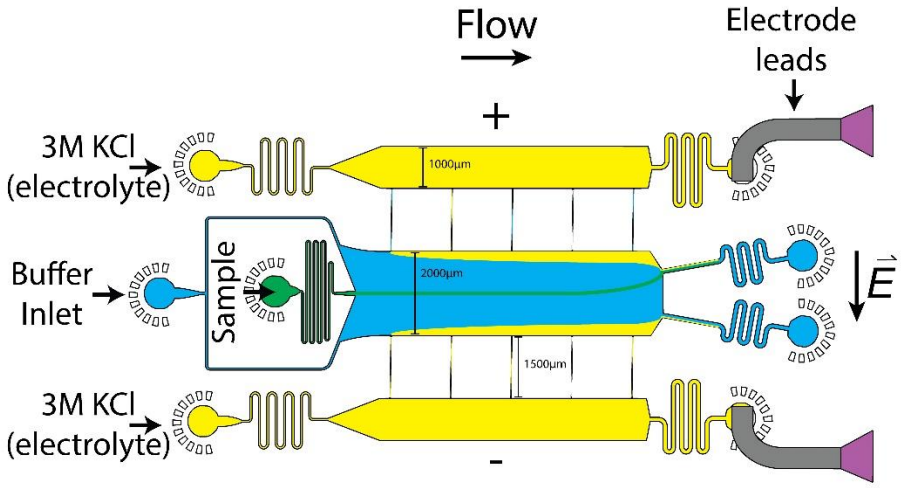

Figure S1. Full schematic of µFFE device. This schematic shows the general design of the 3D µFFE device. The sample is injected through a central port at the beginning of the channel, which is 5 µm tall. Thereby, the sample does not come into contact with any surfaces of the central channel containing co-flow buffer, which is 90 µm tall. Widths of the central chamber and electrolyte chambers, as well as the electrolyte bridge length are indicated on the schematic. The 3 M KCl solution acts as an electrolyte and flows along the edges of the central channel to allow the voltage to be transmitted from the outlet ports to the sample where an electric field is induced opposite to the direction of flow. Further description of the usage and design of the device is given in the text.

Optical detection in µFFE experiments. Images were acquired using an inverted fluorescence microscope (Zeiss AxioObserver D1) equipped with a high-sensitivity electron-multiplying charge-

coupled device (EMCCD) camera (Evolve 512, Photometrics). In experiments with FUS, an appropriate filter set for EGFP detection was used (49002, Chroma Technology). Exposure times were around ~10 ms for each image, allowing for between 30–100 particles to be imaged per frame, and 500–2000 to be imaged per experimental µFFE run. Due to high amounts of free PR_{25} monomer in solution, images for the PR_{25} system were captured in bright-field mode with a phase contrast ring (Ph2). The movement of the droplets in the microfluidic chip was collected by running samples containing the phase-separated droplets into the main chamber of the device and taking images approximately at the coordinate corresponding to the 4th electrolyte bridge (*i.e.*, approx. after 4 s of travel within the chip). At each voltage, a series of images were taken in order to detect ~500–2000 droplets.

Data analysis and calculation of zeta potentials. Images taken in µFFE experiments were analyzed using the Fiji/ImageJ data processing software. The coordinates of condensates were detected using the TrackMate package (*8*), which returned the x,y-coordinates of individual droplets within the channel, with x being the coordinate in the direction of the length of the channel (*i.e.*, flow direction) and y being the coordinate in the direction of its width (*i.e.*, perpendicular to the flow). By calibrating the position of the image within the channel, the travelled distance in x,y-direction over a stream of images was determined, which subsequently gave the residence time, t_r, needed for drift velocity calculations (*i.e.*, the lateral and longitudinal movement of droplets in time). Accordingly, the drift velocity, v, was calculated from the vertical displacement of each condensate, referred to as Δy, according to

$$v = \frac{\Delta y}{t_r}$$

Δy is quantified as the vertical displacement of each condensate from the average vertical coordinate of the stream at 0 V, and t_r was calculated from the flow rate, the x coordinate (or distance traveled), and the known dimensions of the channel. Note, given that the sample stream height is <5% of the height of the total channel and the co-flow buffer flow rate is 50 times higher than the sample flow rate, not much broadening of the signal from the parabolic flow profile is to be expected, which would occur mainly near the edges of the device and may cause velocity variations across the channel.

With v at hand, the electrophoretic mobility, μ, was calculated as

$$\mu = \frac{v}{E_{\text{eff}}}$$

where E_{eff} is the effective electric field across the main electrophoresis channel. E_{eff} is equivalent to V_{eff}/w, with V_{eff} being the effective voltage and w being the width of the device, and was obtained through calibration of each device with 3 M KCl as shown in Figure S2B.

In order to determine V_{eff}, first the resistances R were determined according to Ohm's law $R = V/I$ for each point shown in Figure S2B. By filling the device with 3 M KCl, the internal resistance is effectively zero; therefore, the resistance of the electrode, $R_{elect} = V_{app}/I$, could be determine from the 3 M KCl calibration measurement. Similarly, the resistance of the entire device could be determined during the sample measurement according to the relation, $R_{dev} = V_{app}/I$.

With the resistances R_{elect} and R_{dev} at hand, the resistance of only the internal measurement chamber could be calculated as $R_{main} = R_{dev} - R_{elect}$. Thereby, the voltage drop within the main chamber, expressed as a percentage drop could be calculated as the ratio $eff_V = R_{main}/R_{dev}$. Typically, electrical resistances of 115 and 100 kΩ were determined for R_{dev} and R_{elect}, respectively, and we obtained voltage efficiencies varying from 2% to 12%. From this, V_{eff} could be calculated according to $V_{eff} = eff_V \times V_{app}$, where V_{app} is the applied voltage at the respective sample measurement. This allowed E_{eff} to be determined and therefore the mobility μ of the droplets to be calculated as described.

The measured electrophoretic mobilities for each condensate could then be converted into the zeta potential, ζ, according to the following relation using a modified version of Henry's function (*9*)

$$\zeta = \frac{\mu\eta}{\varepsilon\varepsilon_0}$$

In this relation, ε is relative permittivity of the solution, ε_0 is the permittivity of a vacuum, and η is the dynamic viscosity of the solution. The solution was treated as water, thus the accepted value of $\varepsilon = 78.5$ (*10*) and $\eta = 1.0518\text{x}10^{-3}$ Pa s (*11*) were used. All calculations were all carried out in Python using the integrated development environment Spyder.

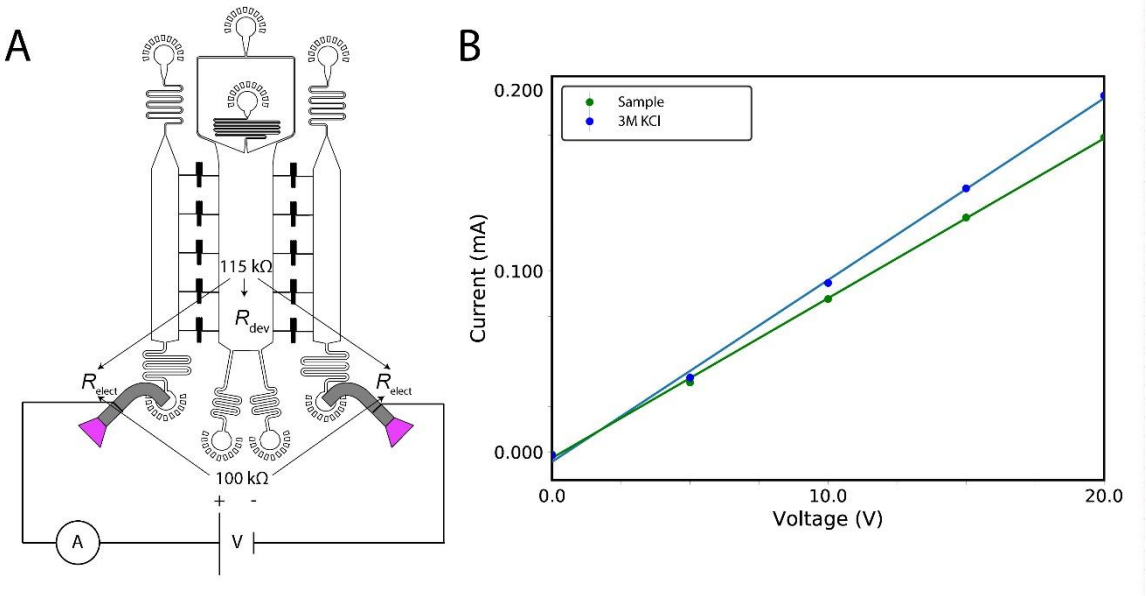

Figure S2. Electrical circuit and calibration of device. (A) Circuit schematic displays how the voltage is applied across the μFFE device and indicates the two sources of voltage drop (high electrical resistance), the electrodes (R_{elect}) and the device itself (R_{dev}). **(B)** Plot displaying the electrical current transmitted through the device both with the sample present (green) and when the device was filled with 3 M KCl solution (blue). Error bars of three measurements at each voltage are smaller than the marker size. This plot allows for the calibration of the voltage efficiency as described in the text.

Supplementary Results

Size dependence of zeta potential. The size of the condensates could not be determined from μFFE experiments because condensates were under flow and appeared blurred in the images due to the 10 ms exposure time. Thus, the size versus zeta potential relationship had to be derived by secondary means. First, static epifluorescence images of FUS condensates were taken. This analysis showed that there is a weak correlation between the total fluorescence intensity (I_T) and the radius (r) of FUS condensates (Figure S3A). In a second step, I_T and zeta potential were derived from images taken during μFFE experiments (Figure S3B). Building on the weak correlation between I_T and r, these data suggest that is no correlation between the zeta potential and I_T, thus indicating that there is no correlation between size and zeta potential.

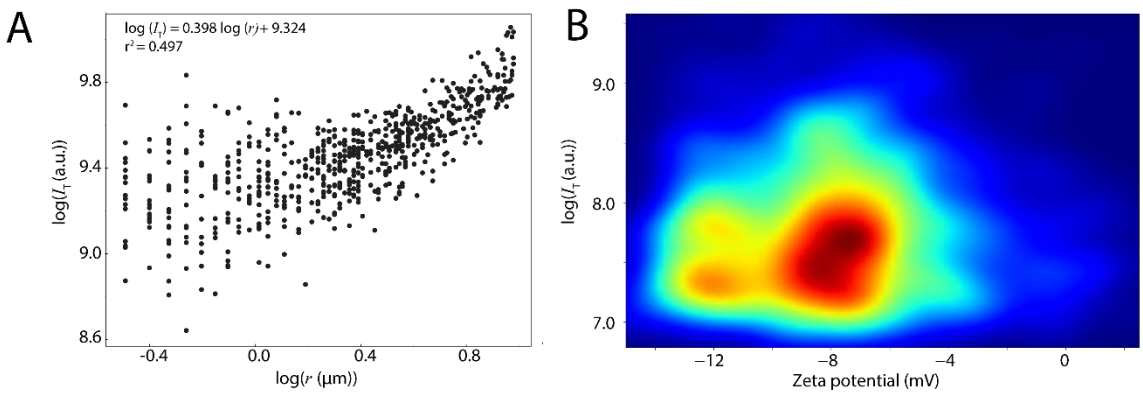

Figure S3. Size dependence of zeta potential. (A) Log–log plot of radius, *r*, versus total fluorescence intensity, I_T, of individual FUS condensates at 6 μM FUS in 50 mM TRIS-HCl at pH 7.4 and 50 mM KCl. *r* and I_T were detected with the TrackMate package in the FIJI image processing software on still images. The correlation between *r* and I_T of the condensates was fitted with a log model. **(B)** 2D plot of zeta potential versus I_T of individual FUS condensates. The plot shows that condensates with varying zeta potentials have similar distributions of I_T, indicating a lack of correlation between zeta potential and size of condensates.

Colloid control measurements. As a control, the zeta potential of 60 nm gold nanoparticles was analyzed using the same microfluidic method as for protein condensate measurements. It was observed that the zeta potential distribution of gold nanoparticles is narrow compared to the distribution of condensates, with the relative standard deviation amounting to only 8% and 20% of that of protein samples. Moreover, there were less broad tails to the distribution in the nanoparticles, which is consistent with the fact that the nanoparticles are monodisperse in size and composition. Note that the nanoparticles are at least an order of magnitude smaller than the condensate systems studied here; hence, due to diffusion effects, the width of the zeta potential distribution of 60 nm gold nanoparticles is likely broader than that of monodisperse particles which are similar in size as condensates.

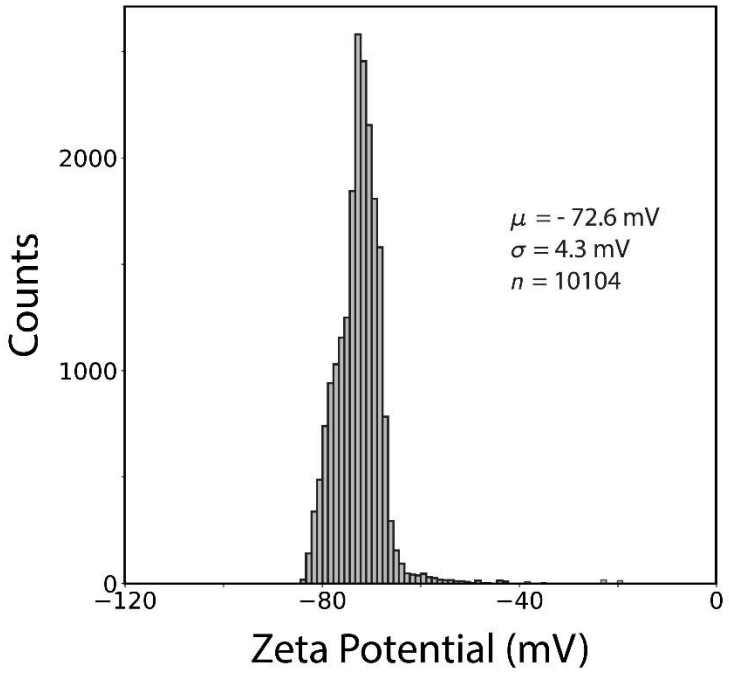

Figure S4. Zeta potential measurement of 60 nm gold nanoparticles. The zeta potential of monodispersed 60 nm gold nanoparticles were measured using the same 3D microfluidic method as for protein condensate measurements.

Supplementary Computational Methods

Coarse-grained protein model. To model the condensation of FUS and PR_{25}, we used a reparameterization of the sequence-dependent coarse-grained model of the Mittal group (*12*) that includes enhanced cation–π interactions (*13*). The model treats each amino acid residue as a single bead. Intrinsically disordered regions are modeled as flexible polymers, with inter-residue bonds described using a harmonic potential. Globular regions are treated as rigid bodies. A Coulombic term with Debye–Hückel electrostatic screening was used for long-range electrostatics, while a knowledge-based potential, termed HPS, that is based on a hydrophobicity scale for amino acids developed earlier (*14*) was used to describe pairwise hydrophobic interactions. We have scaled down the set of HPS parameters by 30% to account for the 'buried' amino acids contained in the globular "rigid" domains. The model was validated by ensuring that we obtained reasonable qualitative agreement with experiments probing phase behavior of FUS wild type versus FUS prion-like domain (PLD); these experiments reveal a greater propensity for LLPS in the former.

Initial atomistic models for coarse-grained simulations. We modelled the full length FUS protein based on Unitprot code K7DPS7 (526 residues, 24 proteins) and a reduced version of the PR_{25} protein (12 Arg

and 13 Pro residues alternately positioned, 200 proteins). We developed an atomistic model of FUS by attaching the disordered regions to the resolved structural domains (residues 285–371 (PDB code: 2LCW) and residues 422–453 (PDB code: 6G99)). Initial intrinsically disordered models for PR25 were developed in PyMol (*15*).

Minimal coarse-grained model for PolyU. We modelled PolyU (30 strands of 80 nucleotides each) as a flexible polymer that represents each nucleotide as a single bead. Inter-residue bonds were described using a rigid harmonic spring, and long-range electrostatics were modelled using a Coulombic term with Debye–Hückel electrostatic screening plus dispersive interactions. Each bead was assigned a charge of –1 and the HPS set of parameters for Glu dispersive interactions.

Coarse-grained simulation methods. We performed direct coexistence simulations at constant volume and temperature to describe the formation of liquid condensates in the different systems. The direct coexistence method consists of simulating both the condensate and diluted phases in the same box separated by an interface. These initial simulation boxes containing both phases were prepared by running simulations at constant temperature and a pressure of 1 bar, using the Berendsen barostat, and then enlarging the simulation box in one direction ~3.5 times. The simulation temperatures were chosen at $T/T_c \sim 0.875$, that is T = 350 K for full length FUS and T = 440 K for PR_{25} with polyU. We ran ~2 μs of molecular dynamics simulations using a Langevin thermostat with relaxation time of 5 ps and a time step of 10 fs (*16*). The LAMMPS software molecular dynamics package was used to carry out all the coarse-grained simulations (*17*).

Surface tension calculation. We determine the surface tension of both condensates at $T/T_c \sim 0.875$, by employing the Kirkwood-Buff expression given in Refs. (*18*, *19*). Our direct coexistence simulations stabilizes two condensate interfaces; thus, the expression for computing the surface tension (γ) is: $\gamma = L_z / 2 \cdot (p_n - p_t)$, where L_z is the length of the box perpendicular to the interface, p_n is the normal component of the pressure tensor perpendicular to the interface (here p_{zz}) and p_t is the average of the tangential components of the pressure tensor (here $(p_{xx} + p_{yy}) / 2$) (*20*).

Back-mapping from coarse grained to atomistic scale. Starting from equilibrium coarse-grained structures of the condensates **(*Step 1 of our multiscale procedure*)**, we built atomic resolution systems following three additional steps. ***Step 2***: We unwrapped the coarse-grained bead coordinates across the periodic boundaries and defined the unwrapped bead positions as coordinates for the amino-acid Cα atoms. Using the tleap module of Amber16 (*21*), we added the missing sidechain and backbone atoms in

random orientations. ***Step 3***: Because adding atoms in this way results in significant atomic overlaps that cannot be resolved through standard energy minimization procedures, we mapped these atomistic configurations to the higher-resolution coarse grained model Martini (*22*) and standard Martini Water (*23*). For nucleic acids, the 'soft' Martini parameters (*24*) without elastic bonds were used. The system's energy was then minimized in the Martini resolution for 5000 steps using the steepest descent algorithm. ***Step 4***: Finally, the program "backward" (*25*) was used to backmap the Martini configuration to the atomistic resolution.

Atomistic molecular dynamics simulations. After back-mapping, we solvated the atomistic condensates using the Gromacs 2018 command gmx solvate (*26*) with the modified TIP3P water model (*27*) creating a rectangular box with the long side (*z*-direction) 12.5 nm away from the condensate interface. We then added Na^+/Cl^- ions at an initial concentration of 0.2 M using the parameters of Beglov and Roux (*28*) together with the nbfix changes of Luo and Roux (*29*) and Venable et al. (*30*). We used the Charmm36M force field (*31*, *32*), which is one of the standard force field combinations for proteins and nucleic acids in explicit solvent and ions. For the FUS system, this resulted in a system of dimensions 12x12x65 nm with 24 protein molecules (170160 atoms), 250095 water molecules, and 900 Na^+ and 1236 Cl^- ions. For the PR_{25}:PolyU system, this resulted in a system of dimensions 7x7x52 nm with 45 protein molecules (21285 atoms), 14 PolyU chains (40 nucleotides, 17906 atoms), 76885 water molecules , and 283 Na^+ and 277 Cl^- ions. All the systems were electro-neutral. Molecular dynamics simulations were performed with Gromacs 2018 (*26*) using the SETTLE algorithm (*33*) to constrain bond lengths and angles of water molecules and P-LINCS for all other bond lengths, which allowed for a time step of 2 fs to numerically integrate the equations of motions. Temperatures were maintained at 300 K using the v-rescale thermostat (*34*) and the pressure at 1 bar using the Parrinello-Rahman barostat (*35*). Long range electrostatic interactions were calculated using the Particle Mesh Ewald (PME) algorithm (*36*) with a cut-off of 1.0 nm. We first performed a short 25-ns long pre-equilibration molecular dynamics simulation, then after absorption of ions into the condensed phase, the concentration of ions in the diluted phase was verified and adjusted back to 0.2 M NaCl by addition/removal of ions or water molecules. We then conducted a 150 ns long molecular dynamics simulation to investigate the distribution of ions within the condense and diluted phases. The trajectories were analyzed using a combination of Gromacs tools and Python MDAnalysis scripts (*37*). For the calculation of partial densities of atoms across the long box axis, the Cα atoms of the system were first centered within the box and the *density* module of Gromacs was used. For the calculation of interaction preferences, two residues were assumed to be in contact if the minimum

distance between their constituent atoms were <3.0 Å in the atomistic resolution and 6.5 Å in the CG resolution. For the calculation of domain interactions, the contacts of all the domain's constituent residues were summed and normalized by the domain's length. The trajectories were visualized using VMD (*38*), Pymol (*15*), and Ovito (*39*).

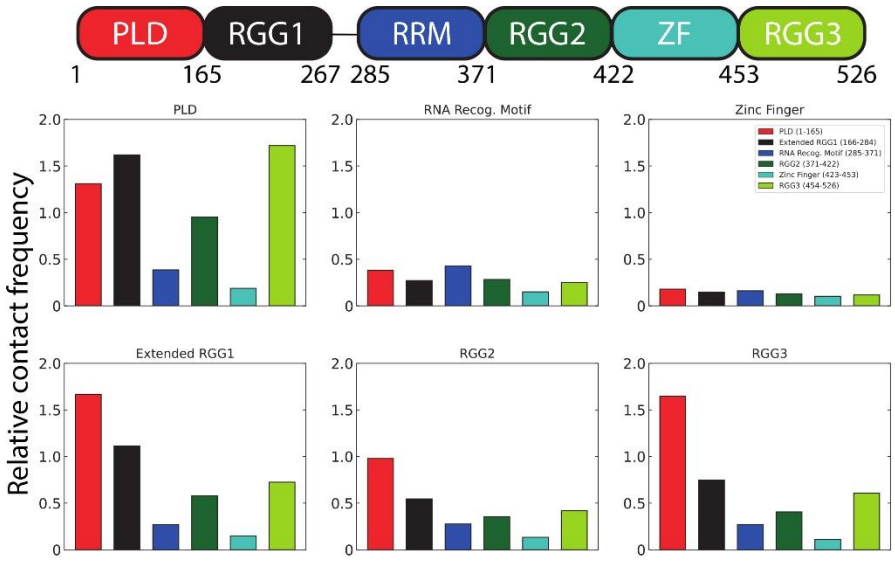

Figure S5. Contacts between FUS domains in condensates. Contact maps showing the relevance of inter-region interactions for each region in FUS (as indicated) within FUS condensates. The bars show the number of inter-protein contacts (amino acids closer than a cut-off of 0.65 nm) mediated by each FUS region normalized by the maximum number of contacts among regions.

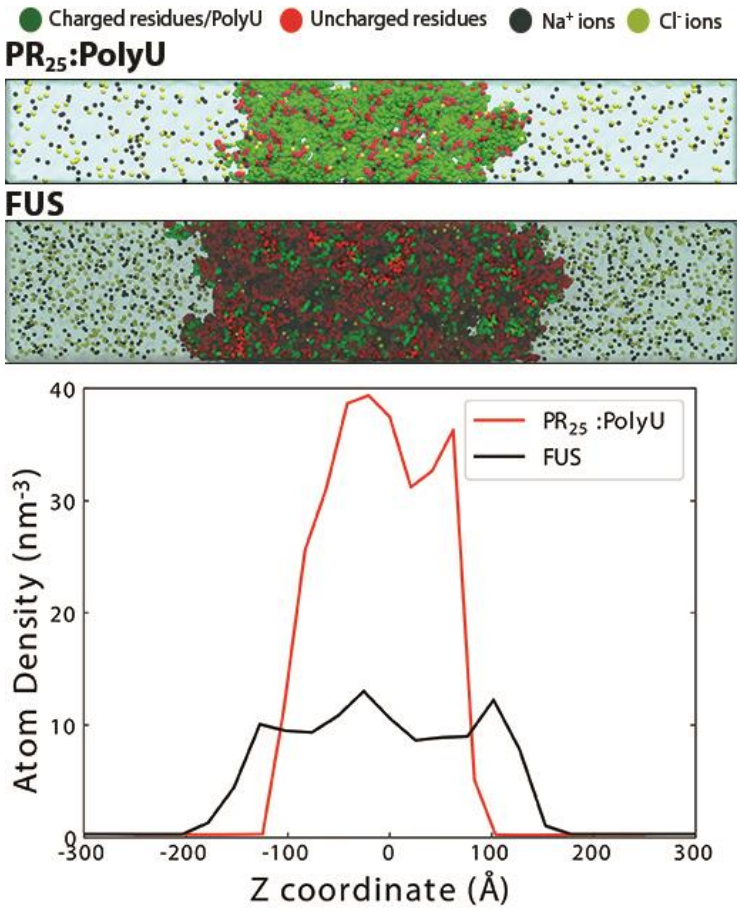

Figure S6. Density of charged atoms in PR_{25}:PolyU and FUS condensates. Total number of charged species (*i.e.*, charged atoms and ions) per unit volume (nm^{-3}) normalized by the total number of atoms (including ions and water) in each system, as a function of the Z axis. Density profiles were computed from equilibrated atomistic simulations. Snapshots of each system are included in the top panel.

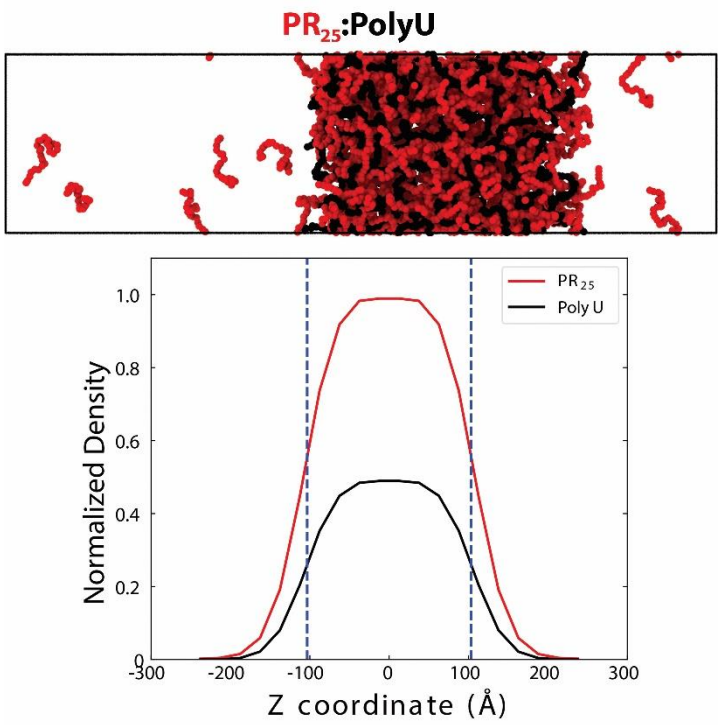

Figure S7. Structure of PR_{25}:PolyU condensates. Normalized densities of individual components (*i.e.*, PR_{25} and PolyU) in PR_{25}:PolyU condensates, along the Z coordinate axis. Density profiles suggest that PR_{25} molecules form a monolayer near the condensate interface lowering the condensate surface tension. A snapshot of the system is provided in the top panel.

Table S1. Diffusion rates and mobility ratios of ions in condensates. To estimate the differential behavior of ions in and around FUS and PR_{25}:PolyU condensates, we measured diffusion coefficients of ions in the condensed ($D_{condensate}$) versus the diluted phase ($D_{diluted}$) for both systems. The values are calculated from a linear fit of the Mean Square Displacements (MSD) exhibited by the different ions in each phase. The time intervals for the calculation of diffusion coefficients (10 ns) was chosen as the longest interval that minimized intermixing of ions in the condensed phase with ions in the diluted phase. The error estimates are calculated as the difference in diffusion coefficients obtained from two time intervals.

System	Ions	$D_{condensate}$ (10^{-5} cm^2/s)	$D_{diluted}$ (10^{-5} cm^2/s)	Mobility Ratio $\left(D_{condensate}/D_{diluted}\right)$
PR_{25}:PolyU	Na^+	0.866 ± 0.34	2.269 ± 0.15	0.38
	Cl^-	1.080 ± 0.37	2.983 ± 0.66	0.36
FUS	Na^+	0.511 ± 0.07	2.185 ± 0.45	0.23
	Cl^-	0.483 ± 0.12	3.226 ± 0.24	0.15

Supplementary References

1. K. L. Saar, Y. Zhang, T. Müller, C. P. Kumar, S. Devenish, A. Lynn, U. Łapińska, X. Yang, S. Linse, T. P. J. Knowles, On-chip label-free protein analysis with downstream electrodes for direct removal of electrolysis products. *Lab Chip*. **18**, 162–170 (2018).

2. W. E. Arter, J. Charmet, J. Kong, K. L. Saar, T. W. Herling, T. Müller, U. F. Keyser, T. P. J. Knowles, Combining Affinity Selection and Specific Ion Mobility for Microchip Protein Sensing. *Anal. Chem.* **90**, 10302–10310 (2018).

3. K. L. Saar, T. Muller, J. Charmet, P. K. Challa, T. P. J. Knowles, Enhancing the Resolution of Micro Free Flow Electrophoresis through Spatially Controlled Sample Injection. *Anal. Chem.* **90**, 8998–9005 (2018).

4. T. W. Herling, T. Müller, L. Rajah, J. N. Skepper, M. Vendruscolo, T. P. J. Knowles, Integration and characterization of solid wall electrodes in microfluidic devices fabricated in a single photolithography step. *Appl. Phys. Lett.* **102**, 184102 (2013).

5. Y. Xia, G. M. Whitesides, Soft lithography. *Annu. Rev. Mater. Sci.* **28**, 153–184 (1998).

6. P. K. Challa, T. Kartanas, J. Charmet, T. P. J. Knowles, Microfluidic devices fabricated using fast wafer-scale LED-lithography patterning. *Biomicrofluidics*. **11**, 014113 (2017).

7. S. H. Tan, N. T. Nguyen, Y. C. Chua, T. G. Kang, Oxygen plasma treatment for reducing hydrophobicity of a sealed polydimethylsiloxane microchannel. *Biomicrofluidics*. **4**, 32204 (2010).

8. J. Y. Tinevez, N. Perry, J. Schindelin, G. M. Hoopes, G. D. Reynolds, E. Laplantine, S. Y. Bednarek, S. L. Shorte, K. W. Eliceiri, TrackMate: An open and extensible platform for single-particle tracking. *Methods*. **115**, 80–90 (2017).

9. J. W. Swan, E. M. Furst, A simpler expression for Henry's function describing the electrophoretic mobility of spherical colloids. *J. Colloid Interface Sci.* **388**, 92–94 (2012).

10. C. G. Malmberg, A. A. Maryott, Dielectric constant of water from 0 to 100 C. *J. Res. Natl. Bur. Stand. (1934).* **56**, 2641 (1956).

11. J. Kestin, M. Sokolov, W. A. Wakeham, Viscosity of liquid water in the range -8°C to 150°C. *J. Phys. Chem. Ref. Data*. **7**, 941–948 (1978).

12. G. L. Dignon, W. Zheng, Y. C. Kim, R. B. Best, J. Mittal, Sequence determinants of protein phase behavior from a coarse-grained model. *PLoS Comput. Biol.* **14**, e1005941 (2018).

13. S. Das, Y.-H. Lin, R. M. Vernon, J. D. Forman-Kay, H. S. Chan, *arXiv*, in press (available at http://arxiv.org/abs/2005.06712).

14. L. H. Kapcha, P. J. Rossky, A simple atomic-level hydrophobicity scale reveals protein interfacial structure. *J. Mol. Biol.* **426**, 484–498 (2014).

15. Schrödinger, LLC, "The {PyMOL} Molecular Graphics System, Version~1.8" (2015).

16. J. S. Rowlinson and B. Widom, *Molecular Theory of Capillarity* (Clarendon Press, Oxford, 1982).

17. S. Plimpton, Fast parallel algorithms for short-range molecular dynamics. *J. Comput. Phys.* **117**, 1–19 (1995).

18. R. C. Tolman, The effect of droplet size on surface tension. *J. Chem. Phys.* **17**, 333–337 (1949).

19. J. S. Rowlinson, B. . Widom, *Molecular Theory of Capillarity* (1982).

20. J. R. Espinosa, A. Garaizar, C. Vega, D. Frenkel, R. Collepardo-Guevara, Breakdown of the law of rectilinear diameter and related surprises in the liquid-vapor coexistence in systems of patchy particles. *J. Chem. Phys.* **150**, 224510 (2019).

21. D. A. Case, T. E. Cheatham, T. Darden, H. Gohlke, R. Luo, K. M. Merz, A. Onufriev, C. Simmerling, B. Wang, R. J. Woods, The Amber biomolecular simulation programs. *J. Comput. Chem.* **26**, 1668–1688 (2005).

22. L. Monticelli, S. K. Kandasamy, X. Periole, R. G. Larson, D. P. Tieleman, S. J. Marrink, The MARTINI coarse-grained force field: Extension to proteins. *J. Chem. Theory Comput.* **4**, 819–834 (2008).

23. S. O. Yesylevskyy, L. V. Schäfer, D. Sengupta, S. J. Marrink, Polarizable water model for the coarse-grained MARTINI force field. *PLoS Comput. Biol.* **6**, 1–17 (2010).

24. J. J. Uusitalo, H. I. Ingólfsson, P. Akhshi, D. P. Tieleman, S. J. Marrink, Martini Coarse-Grained Force Field: Extension to DNA. *J. Chem. Theory Comput.* **11**, 3932–3945 (2015).

25. T. A. Wassenaar, K. Pluhackova, R. A. Böckmann, S. J. Marrink, D. P. Tieleman, Going

backward: A flexible geometric approach to reverse transformation from coarse grained to atomistic models. *J. Chem. Theory Comput.* **10**, 676–690 (2014).

26. M. J. Abraham, T. Murtola, R. Schulz, S. Páll, J. C. Smith, B. Hess, E. Lindah, Gromacs: High performance molecular simulations through multi-level parallelism from laptops to supercomputers. *SoftwareX*. **1**–**2**, 19–25 (2015).

27. J. Huang, S. Rauscher, G. Nawrocki, T. Ran, M. Feig, B. L. De Groot, H. Grubmüller, A. D. MacKerell, CHARMM36m: An improved force field for folded and intrinsically disordered proteins. *Nat. Methods*. **14**, 71–72 (2016).

28. D. Beglov, B. Roux, Finite representation of an infinite bulk system: Solvent boundary potential for computer simulations. *J. Chem. Phys.* **100**, 9050 (1994).

29. Y. Luo, B. Roux, Simulation of osmotic pressure in concentrated aqueous salt solutions. *J. Phys. Chem. Lett.* **1**, 183–189 (2010).

30. R. M. Venable, Y. Luo, K. Gawrisch, B. Roux, R. W. Pastor, Simulations of anionic lipid membranes: Development of interaction-specific ion parameters and validation using NMR data. *J. Phys. Chem. B.* **123**, 9066–9079 (2013).

31. K. Hart, N. Foloppe, C. M. Baker, E. J. Denning, L. Nilsson, A. D. MacKerell, Optimization of the CHARMM Additive Force Field for DNA: Improved Treatment of the BI/BII Conformational Equilibrium. *J. Chem. Theory Comput.* **8**, 348–362 (2011).

32. E. J. Denning, U. D. Priyakumar, L. Nilsson, A. D. MacKerell, Impact of 2′-hydroxyl sampling on the conformational properties of RNA: Update of the CHARMM all-atom additive force field for RNA. *J. Comput. Chem.* **32**, 1929–1943 (2011).

33. S. Miyamoto, P. A. Kollman, Settle: An analytical version of the SHAKE and RATTLE algorithm for rigid water models. *J. Comput. Chem.* **13**, 952–962 (1992).

34. G. Bussi, D. Donadio, M. Parrinello, Canonical sampling through velocity rescaling. *J. Chem. Phys.* **126**, 014101 (2007).

35. M. Parrinello, A. Rahman, Polymorphic transitions in single crystals: A new molecular dynamics method. *J. Appl. Phys.* **52**, 7182 (1981).

36. U. Essmann, L. Perera, M. L. Berkowitz, T. Darden, H. Lee, L. G. Pedersen, A smooth particle

mesh Ewald method. *J. Chem. Phys.* **103**, 8577 (1995).

37. N. Michaud-Agrawal, E. J. Denning, T. B. Woolf, O. Beckstein, MDAnalysis: A toolkit for the analysis of molecular dynamics simulations. *J. Comput. Chem.* **32**, 2319–2327 (2011).

38. W. Humphrey, A. Dalke, K. Schulten, VMD: Visual molecular dynamics. *J. Mol. Graph.* **14**, 33–38 (1996).

39. A. Stukowski, Visualization and analysis of atomistic simulation data with OVITO-the Open Visualization Tool. *Model. Simul. Mater. Sci. Eng.* **18**, 015012 (2010).